

Article

Fluorination Strategies for Mn₃O₄ Nanoparticles: Enhancing Reversibility and Capacity in Li-Ion Batteries

Régis Porhie¹, Batiste Clavier^{1,*}, Taylan Karakoç², Sergey Pronkin², Dominique Foix^{3,4}, Elodie Petit¹, Malika El-Ghozzi¹ and Katia Guérin^{1,*}

¹ Institut de Chimie de Clermont-Ferrand, Université Clermont Auvergne, CNRS, Clermont Auvergne INP, UMR 6296, 24 Av. Blaise Pascal, 63178 Aubière, France; regis.porhie@uca.fr (R.P.); elodie.petit@uca.fr (E.P.); malika.el-ghozzi@uca.fr (M.E.-G.)

² Institut de Chimie et Procédés pour l'Energie, l'Environnement et la Santé, Université de Strasbourg, CNRS, UMR 7515, 25 Rue Becquerel, 67087 Strasbourg Cedex 02, France; taylan.karakoc@etu.unistra.fr (T.K.); sergey.pronkin@unistra.fr (S.P.)

³ Institut des Sciences Analytiques et de Physico-Chimie pour l'Environnement et les Matériaux, Université de Pau et des Pays de l'Adour, CNRS, UMR 5254, 2 Av. Président Angot, 64053 Pau, France; dominique.foix@univ-pau.fr

⁴ Réseau sur le Stockage Electrochimique de l'Energie, CNRS FR 3459, 15 Rue Baudelocque, 80039 Amiens Cedex 1, France

* Correspondence: batiste.clavier@uca.fr (B.C.); katia.araujo_da_silva@uca.fr (K.G.)

Abstract: Transition metal oxides (TMOs) occupy an increasing share in the search for new electrode materials for Li-Ion batteries. Despite promising electrochemical performances (up to 1000 mAh g⁻¹ in the case of conversion), these materials have poor cyclability linked primarily to hysteresis phenomena. To improve their electrochemical performance, one strategy consists of reducing the particle size. A second strategy relies on the incorporation of fluorine directly into electrode materials to limit the solid–electrolyte interface (SEI). Our study focuses on the impact of fluorination on the electrochemical performance of manganese oxide obtained by solid combustion synthesis (SCS). Two fluorinating agents were used: pure gaseous molecular fluorine F₂ and radical fluorine F[•] through xenon difluoride XeF₂ decomposition. The use of F₂ results in strong fluorination localized primarily at the particle surface while XeF₂ diffuses deeper into the particle, resulting in the removal of residual carbon from the synthesis by combustion. The electrochemical performance of the oxide fluorinated with XeF₂ reaches more than 750 mAh g⁻¹ after 160 cycles, whereas that of the oxide fluorinated by F₂ barely exceeds that of the non-fluorinated oxide, less than 200 mAh g⁻¹ after 200 cycles.

Keywords: Li-ion battery; anode material; manganese oxide; fluorination; electrochemical performance



Academic Editor: Claudio Gerbaldi

Received: 15 December 2024

Revised: 24 January 2025

Accepted: 25 January 2025

Published: 28 January 2025

Citation: Porhie, R.; Clavier, B.; Karakoç, T.; Pronkin, S.; Foix, D.; Petit, E.; El-Ghozzi, M.; Guérin, K. Fluorination Strategies for Mn₃O₄ Nanoparticles: Enhancing Reversibility and Capacity in Li-Ion Batteries. *Batteries* **2025**, *11*, 53.

<https://doi.org/10.3390/batteries11020053>

Copyright: © 2025 by the authors. Licensee MDPI, Basel, Switzerland. This article is an open access article distributed under the terms and conditions of the Creative Commons Attribution (CC BY) license (<https://creativecommons.org/licenses/by/4.0/>).

1. Introduction

The transition toward energy networks based on renewable primary sources is a pressing challenge of our time [1]. Considering the intermittent character of these sources, efficient and reversible energy storage devices must be included in the network. Electrochemical energy storage devices (EESD), particularly batteries and supercapacitors, are indispensable components of such versatile energy networks due to their high reversibility and storage efficiency, compact structure and zero operation emission [2]. Lithium-ion batteries (LIBs) are widely used in portable devices and electric vehicles. Graphite is the main negative electrode material in LIBs thanks to its low cost and good cycling performance [3].

However, its limited specific capacity (372 mAh g^{-1}) and safety concerns when the LIBs are charged at a high rate are the main drawbacks of these materials. In recent years, numerous scientific groups have been searching for new negative electrode materials with better electrochemical performance and improved safety. Among them, transition metal oxides (TMOs) and, more specifically, spinel oxides [4–7] (AB_2O_4 , where B is most commonly a trivalent transition metal and A is a divalent metal) are a promising class of negative electrode materials thanks to their high theoretical specific capacity (up to 1000 mAh g^{-1}) and an adequate operating voltage as negative electrode materials. Manganese (II, III) oxide Mn_3O_4 is a promising negative electrode material thanks to its low cost, low toxicity and high theoretical performance (936 mAh g^{-1}) [8–10]. It has a typical spinel structure where the Mn^{3+} ions occupy the octahedral positions, whereas Mn^{2+} ions are located in the tetrahedral positions. Due to the strong Jahn–Teller effect of the Mn^{3+} ions ($3d^4$), the cubic close-packed lattice formed by the oxygen is tetragonally distorted, thus lowering the symmetry to the tetragonal space group $I4_1/AMD$.

However, TMOs in general and, therefore, Mn_3O_4 suffer from poor cyclability due to very high-volume changes from the negative electrode [11,12] and low electrical conductivity, limiting their electrochemical performance in bulk material [9]. To improve the performance of these materials, several strategies are currently employed, such as the nano structuration of particles [10]. Among all the nano-structuration methods, solution combustion synthesis (SCS) is an effective way to produce TMOs due to its versatility, cost-efficiency and simplicity [13]. SCS consists of the heating of an oxidant (metal nitrate) with an organic fuel such as glucose, glycine or mixed urea, forming a sol–gel solution. This nitrate–fuel mix is then heated at moderate temperatures (300 – 500°C) until spontaneous combustion occurs. Numerous parameters engage in this reaction, which explains why SCS is often considered a versatile method to obtain TMOs [14]. Metallic precursor, organic fuel, metal–fuel ratio and the gelation process are all parameters that control the reaction and the nature of the final product [15–17]. However, one can note that SCS can leave unburned products and poorly ordered carbon such as soot if no further purification is performed [15]. Fluorine, due to its unique oxidizing properties, is widely used as a purification process in microelectronics, mostly as NF_3 [18] and CF_4 [19]. Hydrofluoric acid (HF) is also a common wet cleaning agent in silicon wafer manufacturing, which effectively removes SiO_2 from the wafer surface [20]. The cleaning properties of fluorine could therefore be used to remove the carbon from the oxide particles obtained by SCS. The reactivity of carbon depends mostly on its hybridization: the more ordered the carbon, the less reactive it is [21–23]. The fluorination of such materials can be performed with numerous reagents, such as elemental fluorine F_2 (gas) or by using solid fluorinating agents such as TbF_4 or XeF_2 [23]. By precisely controlling the fluorination parameters (fluorinating agent, temperature and reaction duration) one can succeed in fluorinating and purifying carbonaceous materials by effectively removing poorly ordered carbon (over-fluorination, gaseous $\text{C}_n\text{F}_{2n+2}$ departure) and grafting fluorine on higher-hybridized carbon [24].

As mentioned above, fluorine is a significant element in Li-ion batteries. It can be found in current liquid electrolytes relying on LiPF_6 salt dissolved in organic solvents, or in the binder of the electrodes with the fluoropolymer PVDF (poly(vinylidene fluoride), $(\text{CH}_2\text{CF}_2)_n$). By using fluorinated additives in electrolytes, the electrochemical performance of Li-ion batteries can be increased by improving the solid electrolyte interface (SEI) [25,26]. Pre-fluorinated negative electrodes are also a way to improve SEI [27,28]. By performing surface fluorination of such electrodes, both their reversibility and their capacity can be significantly improved [29,30]. In the case of Mn_3O_4 , Palaniyandy et al. [31] evaluated the electrochemical performances of fluorinated Mn_3O_4 nanospheres as negative electrode material for Li-ion batteries. They were first synthesized by the calcination of MnO_2 at

850 and 1000 °C. The oxides were then dispersed in an aqueous solution of NH₄F, dried and heat treated at 450 °C under argon (initial F–Mn ratio of 1/3). They demonstrated an increased capacity of up to 80% compared to non-fluorinated oxide after 100 cycles (990 mAh g⁻¹ vs. 553 mAh g⁻¹) at a current density of 100 mA g⁻¹. Direct fluorination by F₂ or fluorination through the decomposition process of a solid fluorinating agent such as XeF₂ applied on oxide nanoparticles prepared by SCS can make it possible to combine the purification process and modification of the electrode material in a single step, and has so far never been studied.

In this work, we will focus on the impact of fluorination on the physicochemical properties of manganese oxide nanoparticles synthesized by SCS. Two fluorinating agents were used: molecular fluorine F₂ and xenon difluoride XeF₂, the generator of radical fluorine F[•]. The electrochemical performances of these materials as negative electrode materials in a conventional coin cell Li-Ion battery will be compared to the non-fluorinated oxide.

2. Materials and Methods

2.1. Synthesis of Manganese Oxide Nanoparticles

Nanoparticles of Mn₃O₄ were synthesized using the modified solution combustion synthesis (SCS) method. The stoichiometric amount of manganese (II) nitrate (Mn(NO₃)₂·4H₂O 98% purity from Merck, Darmstadt, Germany) needed to produce 1 g of Mn₃O₄ was dissolved in 20 mL of ultrapure water (Veolia Chorus Pro, 18.2 MΩ.cm, TOC < 2 ppb) together with ammonium citrate ((NH₄)₃Cit, ACS grade, Merck, Darmstadt, Germany) in a 3:2 molar ratio. Next, the fuel compound glycine (NH₂CH₂COOH, Merck) was added to the same solution in a 1:1 molar ratio concerning Mn nitrate. After the complete dissolution of all components, the solutions were kept for 48 h in an oven at 70 °C under the air for slow evaporation of the solvent. This step results in the formation of a yellowish gel-like mixture. Next, the glass flask was put on the heating plate preheated at 350 °C. Within a minute, a darkening and expansion of gel inside the flask was detected, ended by its sudden combustive decomposition, resulting in the formation of a fine brown powder of Mn₃O₄. The glass flask was rinsed with ultrapure water and the powder was filtered and thoroughly washed with water on the filter, then dried in an oven at 80 °C under air for 4 h. After cooling down, the final powder mass was measured and the yield was calculated. The typical yield of the synthesis was between 70 and 90%.

2.2. Fluorination of Manganese Oxide Nanoparticles

Fluorination of Mn₃O₄ oxide nanoparticles with F₂ gas (Mn₃O₄-F₂) was carried out in a 525 mL passivated nickel reactor at 120 °C for 16 h. The samples are first outgassed under vacuum at 100 °C for one hour before being transferred to the fluorination reactor. The reactor is then placed under vacuum at room temperature for one hour using a primary pump (P_{residual} = 0.01 mbar). An intermediate valve, which separates the flow meters and the reactor, is opened, bringing the pressure within the reactor to around 30 mbar, composed of nitrogen N₂ (purge gas). Fluorine is then injected at room temperature at 2 mL/min until a fluorine–manganese ratio of approximately 0.10 is reached. Precise control of the quantity of fluorine injected is difficult due to uncontrolled injection in the first 10 s when the flow meter is switched on. The system is then left in balance for approximately 20 min before turning on the furnace heating. Once the reaction is complete, the reactor is flushed with nitrogen at 100 mL/min for one hour. The fluorinated samples are first weighed and then stored in a glove box before further characterization.

Xenon difluoride XeF₂ takes the form of a volatile solid at room temperature. It is very reactive to ambient humidity, releasing HF vapors. Fluorination of Mn₃O₄ oxide nanoparticles (Mn₃O₄-XeF₂) with this fluorinating agent took place in a 30 mL Teflon

reactor, prepared in an argon glove box. This reactor was the subject of a preliminary study on its tightness under the same conditions (120 °C, 16 h). In a typical experiment, Mn₃O₄ is weighed and then introduced into the Teflon reactor. After that, a quantity of XeF₂ is weighed in an alumina crucible (F–Mn ratio = 0.1) and introduced into the reactor. The Teflon reactor is closed tightly before being taken out of the glove box before being placed in an oven at 120 °C for 16 h. Once the reaction is complete, the reactor is returned to the glove box and opened to recover the sample.

The fluorination rate of Mn₃O₄ was determined by a fluoride ion selective electrode (F-ISE Metrohm, Herisau, Swiss). Approximately 10 mg of the compound is precisely weighed and then introduced into a 20 mL Teflon reactor. Then, 20 mL of a 20% acetic acid solution is added. The reactors are stirred at room temperature for 15 min and introduced into a microwave mineralizer. Digestion is carried out at 190 °C for 1 h in a Multiwave 5000 microwave digestion platform (Anton Paar, Graz, Austria), allowing the sample to be completely dissolved. The choice of acid was decisive in limiting HF formation (pK_a HF/F[−] = 3.2), which can potentially be released, lowering the real concentration value of F[−] measured. Once the mineralization is complete, 5 mL of the solution is diluted in a 50 mL flask, and then 25 mL of this solution is taken into a polyethylene bottle. An ionic strength buffer is added, and the mixture is stirred for 30 min. The fluoride ion concentration is determined by prior calibration of the fluoride electrode using standard solutions. The fluorination level can then be calculated for each fluorinated oxide by considering the HF/F[−] balance existing in the solution ($pH_{solution}$ = 4.15, reproducible for the two fluorinated oxides: Mn₃O₄-F₂ and Mn₃O₄-XeF₂). The F–Mn ratio was 0.130 in Mn₃O₄-F₂, whereas the F–Mn ratio was only 0.056 in Mn₃O₄-XeF₂.

2.3. Physicochemical Characterization

X-ray diffraction (XRD) patterns were recorded with a PANalytical X'Pert diffractometer equipped with a Cu K_{α1+2} source and a linear detector X-Celerator. Data were collected between 10 and 80° (2θ range) with a 0.0167° step (acquisition time 3 h) and analyzed by the Le Bail method (Full Pattern Matching) [32] using the Fullprof program [33]. Scanning Electron Microscopy (SEM) images were collected with a ZEISS Supra 40 SEM (Oberkochen, Germany) operating at 3 kV. The porosity of the materials was probed by nitrogen adsorption with a Micrometrics ASAP 2020. Specific surface area was then calculated using the Brunauer–Emmett–Teller (BET) method. Analyses were performed with outgassed samples under a secondary vacuum at 40 °C for 24 h. Infrared spectra were collected with a Nicolet Summit X FTIR spectrometer equipped with an Everest Diamond ATR module in the 400–4000 cm^{−1} range. Twenty-five successive scans with a 4 cm^{−1} resolution were performed for each sample. Raman spectra were collected with an inViaTM InSpect confocal Raman microscope (RENISHAW, Wotton-under-Edge, UK) equipped with a charge-coupled device multichannel detector. A 532 nm argon laser was used as the radiation source, with a power of 1 mW. Spectra were recorded using an acquisition time of 60 s. XPS measurements were performed with a THERMO Escalab spectrometer equipped with an argon glove box to prevent contact between samples and the atmosphere. X-ray source was provided by an Al source coupled with a monochromator to keep only Al K α radiation ($E = 1486.6$ eV). High vacuum was applied during analysis (2×10^{-5} Pa). Binding energy was calibrated using the C 1s peak of CH₂- carbons from contamination at 285.0 eV, and spectra were collected with a constant pass energy of 20 eV, recorded several times to ensure that there is no degradation of the samples under X-ray beam. The spectra were fitted using a minimum number of contributions.

2.4. Electrode Preparation, Coin Cell Assembly and Electrochemical Tests

The electrodes containing the active material (i.e., Mn₃O₄ before and after fluorination with F₂ or XeF₂) were obtained by mixing the active material (80% wt.) with conductive carbon (10% wt., Acetylene Black, Strem chemicals, Newburyport, MA, USA, 99.99%) in an agate mortar and pestle. The mixed powder was then dispersed in a viscous solution of PVDF (poly(vinylidene fluoride), MTI) dissolved (2.5% wt.) in NMP (N-Methyl-2-pyrrolidone, Sigma-Aldrich, Saint-Louis, MO, USA 99.5%). The obtained ink was deposited on stainless-steel spacers (1 mm thickness, 16 mm diameter) previously dried for 48 h at 80 °C. The electrodes obtained were further dried in an oven under vacuum for 4 h at 120 °C before entering an Ar-filled glovebox with water content below 1 ppm.

Coin-type cells CR2032 were assembled and, using the casted electrodes as the working electrode and lithium metal disks as the counter electrode (S4R, 99.9%), the electrodes were separated by Celgard/Whatman/Celgard three-layer separator (Celgard®2340, Charlotte, NC, USA,) soaked with 1M LiPF₆ in EC/DEC (1:1) (*v/v*) liquid electrolyte (LP40, Sigma-Aldrich). Galvanostatic cycling and cyclic voltammetry measurements were recorded on VMP and BCS Biologic apparatus in a 20 °C temperature-controlled room. Galvanostatic cycling was performed at a current density of D/20 (46.85 mA g⁻¹), and cyclic voltammetry was conducted at a scan rate of 0.05 mV s⁻¹. C-rate measurements were performed on the active materials after the first five cycles at D/20 to reach a stable reversibility of the cells after the first cycles were affected by the initial irreversibility of the conversion mechanism [34]. EIS measurements were obtained using the assembled CR2032 coin-type cells with LP40 electrolyte and Li metal counter electrode. The EIS spectra were recorded on BCS Biologic apparatus with a Zfit EIS fitting tool at room temperature within a 0.02 Hz–10 kHz frequency range with an amplitude of 10 mV. The cells were allowed to relax for 4 h after assembling and at the end of the discharge reach a stable potential. GITT measurements were also performed on coin-type cells with the same data-collecting apparatus as described above, with repeated 30 min pulse (τ) at 46.85 mA g⁻¹ current density (D/20) followed by 300 min relaxation step.

3. Results and Discussion

3.1. F₂ Fluorination Monitoring

The fluorination reactor is equipped with a pressure sensor, which makes it possible to monitor the evolution of the pressure in the reactor. This evolution is presented in Figure 1. The leak rate is calculated first because it will make it possible to determine the reactivity threshold of the material. Significant work has been carried out to minimize this leak rate (0.81 mbar/h at room temperature) because the quantity of fluorine injected is low (4.74 mbar, or approximately 2 mL of F₂ in STP values). In Figure 1, where the zero abscissa begins at the F₂ injection, we first notice an increase in pressure during the first minute linked to the F₂ injection. The pressure decreases until the oven is turned on, meaning the material reacts with F₂ at room temperature. When the temperature of the furnace rises, the pressure within the reactor naturally increases and follows approximately the temperature rise curve. Once the temperature level is reached, the pressure keeps on increasing slightly due to a slow heat transfer provided mainly by radiation and conduction in the highly depressurized reactor (P = 50 mbar). A pressure plateau is finally reached before a decrease at an exponential rate during the hours following, reaching the temperature plateau. Eight hours after the injection, the pressure begins to rise regularly. This regular increase in pressure is directly linked to the reactor leak rate, which becomes non-negligible given the consumption of residual fluorine by the material.

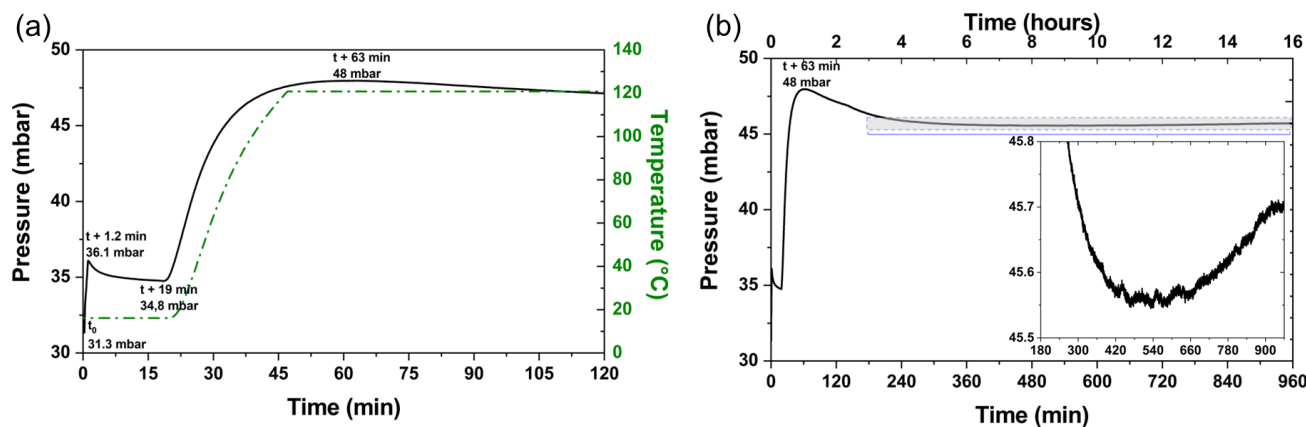


Figure 1. (a) Pressure profile of the fluorination of Mn_3O_4 -based nanoparticles during the first 120 min and (b) during the whole fluorination process under pure molecular fluorine F_2 (960 min, 16 h).

3.2. Characterization of Manganese Oxide Particles

SEM images of the oxides are presented in Figure 2. Non-fluorinated particles develop a strong macroporosity, which originates from the solution combustion synthesis, where a significant volume of gases is released from the combustion of organic species. This macroporosity is then preserved after fluorination. The specific surface area of non-fluorinated Mn_3O_4 particles determined by BET is quite high, around $24 \text{ m}^2/\text{g}$, and decreases by approximately 9% after fluorination with XeF_2 and by 17% after fluorination with F_2 . From these values, the average particle diameter d_{BET} was estimated from a classical spherical model, where $d_{\text{BET}} = \frac{6000}{\rho \times S}$ (d_{BET} in nm, ρ in g/cm^3 and S in m^2/g) varies from 52 to 62 nm, much smaller than what is observed by SEM. Such differences can be explained by the macroporosity of the material only visible by SEM and the strong aggregation of particles between them. The adsorption isotherms presented in ESI (Figure S1) also show that the samples have an appearance similar to a type II isotherm, characteristic of macroporous compounds according to the IUPAC nomenclature [35], with an H3 type hysteresis loop also characteristic of a network consisting essentially of macropores not completely filled by N_2 .

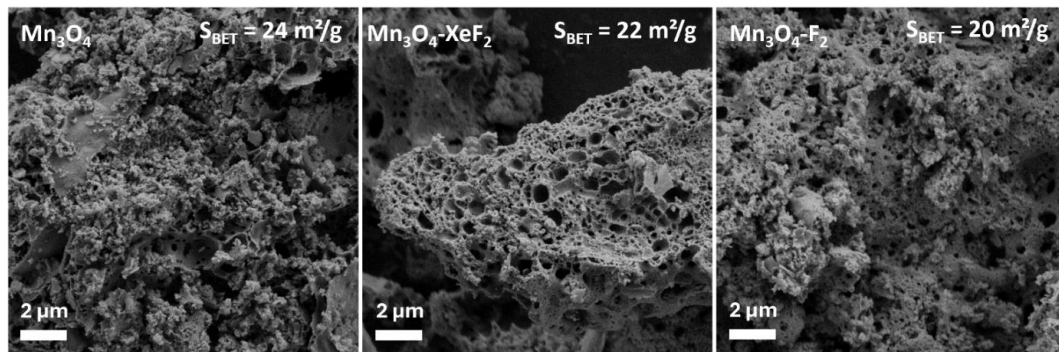


Figure 2. SEM images of Mn_3O_4 -based nanoparticles (non-fluorinated, fluorinated by XeF_2 and fluorinated by F_2).

Figure 3 represents the X-ray diffractograms of Mn_3O_4 (as prepared, fluorinated with XeF_2 and fluorinated with F_2). Most of the peaks of the non-fluorinated oxide can be indexed to the Mn_3O_4 Hausmannite phase (ICSD Collection Code: 68174) [36]. The remaining peaks at 35.1° (shoulder) and 40.7° are assigned to the cubic MnO Manganosite phase (ICSD Collection Code: 9864) [37]. The formation of minor quantities of MnO can

be related to the partial hydrolysis of Mn(II) nitrate during the slow evaporation of the solvent, leading to the formation of $\text{Mn}(\text{OH})_2$, which decomposes into MnO during the combustion process. The hydrolysis is strongly reduced in the presence of citrate due to the formation of a stable Mn(II) citrate complex [38]. X-ray diffractograms can be refined satisfactorily by full-pattern matching using the two previous phases as a starting structural model (Figure S2). The diffraction peaks are relatively broad, which suggests that the crystallites are small. This is confirmed by the estimation of the size of the crystallites by application of Scherrer's formula. Fluorination significantly increases the size of the crystallites, from 18 nm for the non-fluorinated oxide to 30 nm for the oxide fluorinated with XeF_2 or F_2 . By linking these data to those of nitrogen adsorption, we conclude that the nanoparticles are made up of several crystallites. The diffractogram of $\text{Mn}_3\text{O}_4\text{-XeF}_2$ presents numerous similarities with the non-fluorinated oxide, namely the presence of Mn_3O_4 and MnO , without evidence of a fluorinated phase of the MnF_2 type ($I_0 = 100\%$ at $2\theta = 25.83^\circ$; ICSD Collection Code: 9165) [39] or MnF_3 ($I_0 = 100\%$ at $2\theta = 24.52^\circ$; ICSD Collection Code: 17462) [40]. Mn_3O_4 and MnO are also present on the diffractogram of $\text{Mn}_3\text{O}_4\text{-F}_2$. However, one can notice that MnO peaks are significantly weaker than those observed on the X-ray diffractogram of $\text{Mn}_3\text{O}_4\text{-XeF}_2$. It also presents a broad peak of very low intensity centered on 25.91° , which could correspond to the base peak of a very poorly crystallized MnF_2 -type phase. The fluorination of microcrystalline MnO under F_2 at 140°C with an F–Mn ratio between 0.25 and 0.75 was performed by De Windt et al. [41], and an amorphous MnOF_x phase was evidenced. In our case, the F–Mn ratio in $\text{Mn}_3\text{O}_4\text{-F}_2$ was 0.130 and fluorination was performed at 120°C on nanocrystalline $\text{Mn}_3\text{O}_4/\text{MnO}$ particles. The hypothesis of a fluorine-rich phase present on the surface of $\text{Mn}_3\text{O}_4\text{-F}_2$ is reinforced by the XPS analysis by calculating the O–Mn and F–Mn ratios (Table 1). The O–Mn ratio in pristine material is very close to the theoretical ratio (1.31 versus 1.33) and diminishes significantly when the compound is fluorinated with XeF_2 and F_2 (1.20 and 1.00, respectively). The F–Mn ratio is almost 2.5 times higher in $\text{Mn}_3\text{O}_4\text{-F}_2$ (0.61) than in $\text{Mn}_3\text{O}_4\text{-XeF}_2$ (0.25), which confirms that fluorination with F_2 is preferably carried out on the surface of the particles.

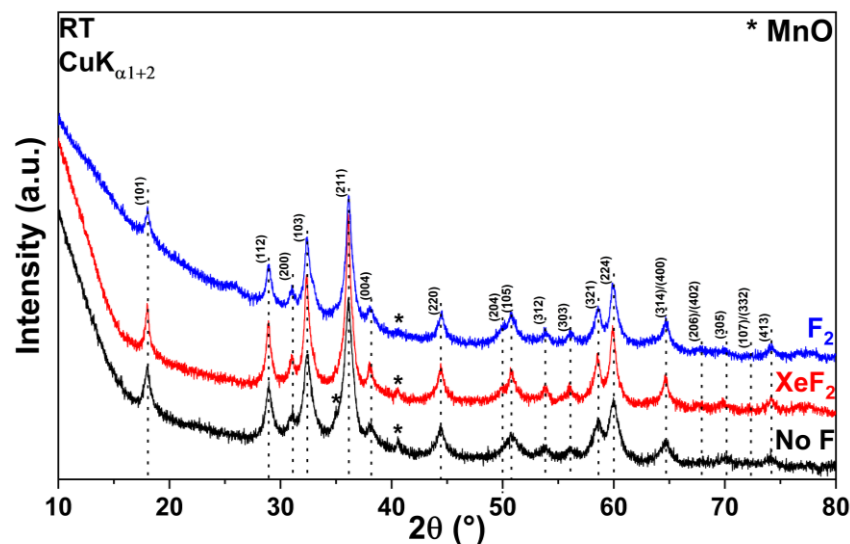


Figure 3. X-ray diffractograms of Mn_3O_4 -based nanoparticles (pristine, fluorinated by XeF_2 and fluorinated by F_2) performed at room temperature. Indexed peaks correspond to Hausmannite phase.

Table 1. Atomic percentage of Mn₃O₄-based nanoparticles (non-fluorinated, fluorinated by XeF₂ and fluorinated by F₂) determined by XPS.

	C	Mn	O (530.1 eV)	F	O/Mn Ratio	F/Mn Ratio
Pristine	26.8	25.9	33.8	-	1.31	-
10% XeF ₂	26	23.2	31.1	5.9	1.20	0.25
F ₂	27.5	25.9	23.1	15.7	1.00	0.61

XPS spectra of Mn 3s and Mn 3p displayed in Figure 4 exhibited a significant shift in Mn 2p peak position to higher energies when fluorination was performed under F₂, from 641.5 eV for Mn₃O₄, very close to the 641.7 eV value as reported by Ardizzone et al. [42], to 642.3 eV for Mn₃O₄-F₂, whereas this energy remains close to pristine material in the case of Mn₃O₄-XeF₂ (641.7 eV). This result was expected, as fluorine is more electronegative than oxygen, thus increasing the binding energies of the manganese. It has already been demonstrated that the value of the Mn 3s exchange splitting is correlated with the valency of Mn. In our case, Mn 3s exchange splitting is 5.6 eV in pristine material, in perfect agreement with Galakhov et al. [43]. This value rises to 5.7 eV in Mn₃O₄-XeF₂ and 5.75 eV in Mn₃O₄-F₂. An increase in the value of the Mn 3s exchange splitting is characteristic of a decrease in the formal valency of Mn in manganese oxides. This observation does not necessarily mean that manganese is reduced under fluorine but rather that fluorination proceeds through a substitution mechanism, whereby few oxygen atoms (−2 valence) are substituted by fluorine atoms (−1 valence), naturally resulting in a small decrease in the formal valency of manganese atoms. This is confirmed by the position of the main F 1s peak centered at 684.7 eV and 685.1 eV in Mn₃O₄-XeF₂ and Mn₃O₄-F₂, respectively, characteristic of a metal–fluorine bond [44]. A second contribution to the F 1s peak at 688.0 eV is observed for Mn₃O₄-F₂ and will be discussed later in the article.

Raman and infrared spectra of the obtained products are presented in Figures 5 and 6, respectively. A strong band occurs in Raman spectroscopy at 640–655 cm^{−1} and at 600 cm^{−1} in infrared spectroscopy in all samples. These bands are characteristic of a spinel structure and are assigned to the A_{1g} and E_u vibration modes in Raman and infrared, respectively, of MnO in tetrahedral sites, in agreement with the literature [45–47]. Raman spectra display a strong variation in the peak position between the different samples: from 647 cm^{−1} for non-fluorinated Mn₃O₄ and Mn₃O₄-XeF₂ to 652 cm^{−1} for Mn₃O₄-F₂. Such variations in peak position have already been reported by Julien et al. [47]. In our case, the slight increase in the Raman shift of the MnO vibration of Mn₃O₄-F₂ goes hand in hand with the shift towards higher energies of the 3s and 3p peaks of manganese on XPS spectrum (Figure 4) compared to pristine Mn₃O₄ and Mn₃O₄-XeF₂. Weaker bands were detected on Raman spectra at 465, 360 and 310 cm^{−1}, in agreement with previous reports [45,47]. The MnO signature, clearly demonstrated by X-ray diffraction (Figure 3), is difficult to observe by Raman spectroscopy. Broad, low-intensity bands should be located around 529 and 1050 cm^{−1} due to phonon vibrations [48]. In our case, the main band of Mn₃O₄ centered on 650 cm^{−1} would mask that of MnO centered on 529 cm^{−1} due to its width, and the one centered on 1050 cm^{−1} is completely absent from our Raman spectra. Fluorinated oxides (Mn₃O₄-XeF₂ and Mn₃O₄-F₂) do not reveal the presence of a phase of MnF₃ (the absence of an intense characteristic band at 511 cm^{−1}, that at 651 cm^{−1} could be confused with that of Mn₃O₄) [40], and the presence of MnF₂ is unlikely as no distinct bands at 476, 341 or 247 cm^{−1} are observed on the Raman spectrum of Mn₃O₄-F₂ [49].

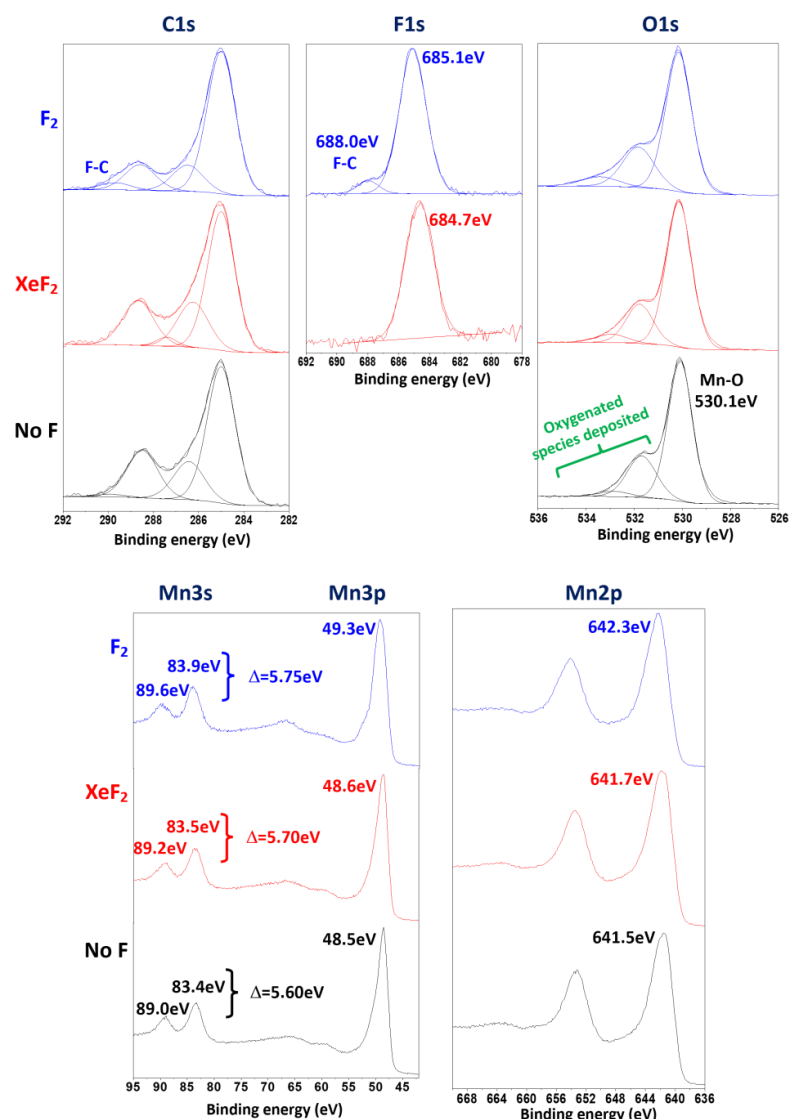


Figure 4. C 1s, F 1s, O 1s and Mn 3s, 3p, 2p XPS spectra of Mn_3O_4 -based nanoparticles (pristine, fluorinated by XeF_2 and fluorinated by F_2).

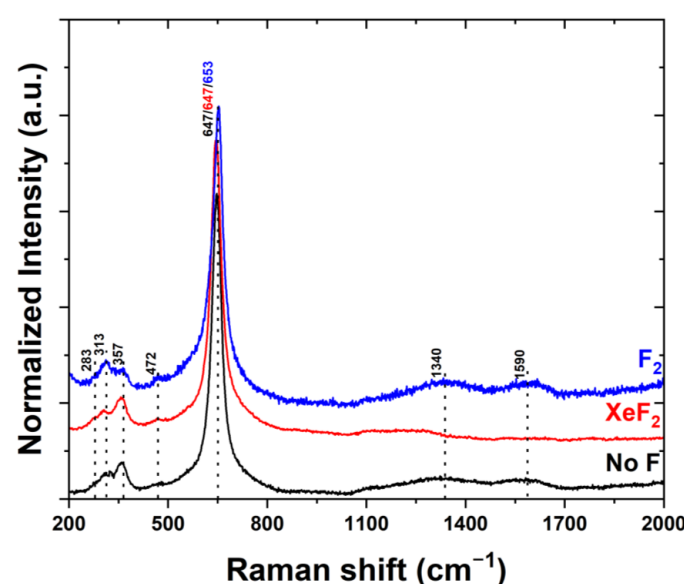


Figure 5. Raman spectra of Mn_3O_4 -based nanoparticles (pristine, fluorinated by XeF_2 and fluorinated by F_2).

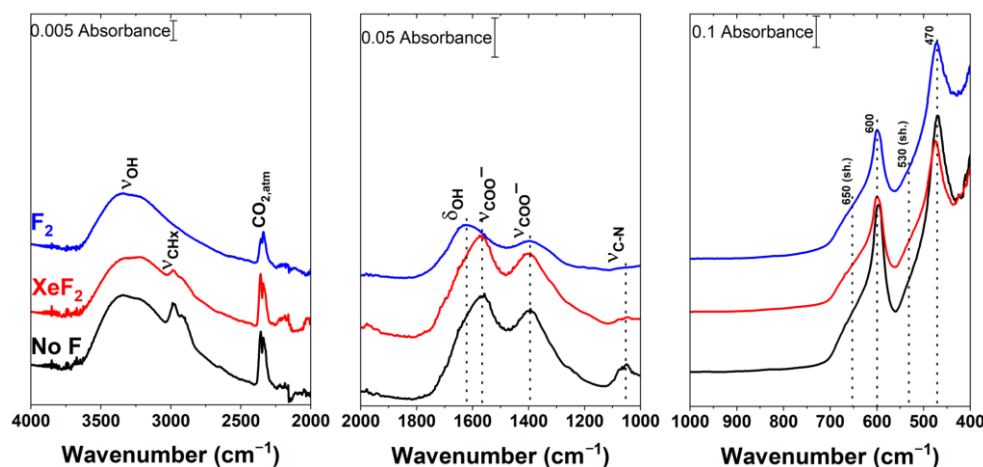


Figure 6. Infrared spectra of Mn_3O_4 -based nanoparticles (pristine, fluorinated by XeF_2 and fluorinated by F_2).

Infrared and Raman spectra also show the presence of bands far from the region where MnO vibrations are registered ($>1000 \text{ cm}^{-1}$). Given the synthesis process (solution combustion synthesis), it is likely that an organic fraction remains unburned or partially burned. The bands centered at 1560 , 1400 and 1056 cm^{-1} in infrared spectra correspond to these two compounds (ammonium citrate and glycine in its zwitterionic form). This hypothesis is reinforced if we look at the 2000 – 4000 cm^{-1} region in infrared spectroscopy (Figure 6) in which the C-H (2800 – 3000 cm^{-1}) bands are visible. Raman spectroscopy (Figure 5) provides information on the presence of poorly ordered carbon [50], materialized by the D-band located at 1355 cm^{-1} and the G-band located at 1580 cm^{-1} . This carbon undoubtedly comes from the combustion of organic matter (glycine and ammonium citrate). Fluorination with XeF_2 and F_2 reduces the infrared and Raman contribution of poorly ordered carbon and organic species, respectively, without totally eliminating them. The Raman spectrum of Mn_3O_4 - XeF_2 sees the carbon contribution (D- and G- bands) virtually disappear compared to pristine material or the one fluorinated with F_2 , but its infrared spectrum still displays a strong organic contribution ($-\text{CH}_x$, $-\text{COO}^-$ and $-\text{C-N}$). This can be explained by the fluorination mechanisms [51], which are not the same between F_2 and XeF_2 . In the case of fluorination with F_2 , the mechanism follows a molecular process in which F_2 molecules interact with the surface of the reagent, thus causing its fluorination. This is confirmed by XPS spectra of the F1s peak of Mn_3O_4 - F_2 , where the fluorine peak presents a small second contribution at 688.0 eV , assigned to a CF_x -type environment [52,53]. However, no $-\text{CF}_x$ bands are observed by infrared spectroscopy in the 1100 – 1200 cm^{-1} region [54]. Unlike F_2 , where fluorine has an oxidation state of $+0$ and is covalently bonded to the second fluorine atom, XeF_2 decomposes into atomic fluorine F^\bullet and gaseous xenon [55,56]. Although these entities are more reactive than F_2 , they are also significantly smaller and can percolate through the bulk material. Another determining parameter in the ability of the fluorinating agent to percolate into the material and thus efficiently remove the poorly ordered carbon is the pressure at which the reaction takes place. In the case of fluorination with F_2 , the injected fluorine pressure was only 4.74 mbar . This low fluorine pressure leads to the adsorption of F_2 at the surface of the particles, which will immediately react, leading to strong surface fluorination as evidenced by XPS. During the fluorination with XeF_2 , it should also be remembered that the preparation took place in a glove box, almost at atmospheric pressure ($P = P_{\text{atm}} + 30 \text{ mbar}$) in a small 30 mL reactor. The partial pressure of XeF_2 is therefore much greater than that in the nickel reactor during the fluorination with F_2 ($P_{\text{XeF}_2} = 130 \text{ mbar}$ for a total pressure of approx. 1500 mbar at 120°C). A final parameter that explains the lower fluorination rate in the case of fluorination with XeF_2 and

the disappearance of carbon from the Raman spectra is its high affinity for radical species. Indeed, poorly ordered carbon is characterized by numerous dangling bonds, which have the same characteristics as a radical. However, XeF_2 is, unlike F_2 , a generator of F^\bullet radicals, which will be able to preferentially attack these sites releasing $\text{CF}_{4(g)}$, reducing the amount of fluorine available to carry out the fluorination of the oxide. This phenomenon also exists in the case of fluorination with F_2 but in a less pronounced manner, where it will react preferentially with the residual organic species (glycine and ammonium citrate) and the oxide Mn_3O_4 . The strong affinity of F^\bullet towards this poorly ordered carbon, larger than that of F_2 , and its ability to percolate to the bulk explain the low level of fluorination of the oxide compared to the one fluorinated with F_2 , both in the whole material (F–Mn ratio measured on 10 mg samples by F-ISE) and at the surface of the particles (F–Mn ratio calculated from XPS spectra).

3.3. Electrochemical Characterization of Mn_3O_4 -Based Nanoparticles and Battery Performance

The obtained materials were finally investigated as active materials for lithium-ion battery negative electrodes. Figure 7a displays the first galvanostatic reduction and oxidation of Mn_3O_4 before and after molecular fluorination by elemental F_2 gas or radical fluorination by XeF_2 decomposition. The initial discharge of the sample fluorinated with XeF_2 shows a 200 mAh g^{-1} excess capacity compared to the non-fluorinated sample and the sample fluorinated with F_2 . However, for such conversion materials with electrochemical activity at low potentials, the obtained capacity for the first cycles is difficult to attribute to an improvement of electrochemical performances, as complex SEI (solid electrolyte interphase) formation mechanisms can contribute to the reduction capacity [57]. The excess capacity originating from an SEI formation is underlined by the first cycle reduction capacities from all the samples being systematically above the theoretical capacity of Mn_3O_4 (i.e., 937 mAh g^{-1}). The following cycles, however, do not experience an excess reduction capacity and are able to reach coulombic efficiencies close to 100%, as can be seen in Figure S3 for galvanostatic profiles of prolonged cycles. The galvanostatic profiles show minor differences for all the materials, displaying a flat reduction plateau at 0.3 V vs. Li^+/Li , consistently with the previously shown XRD, Raman and infrared spectroscopy, with a majority of Mn_3O_4 spinel structure being maintained after fluorination. Further investigation of the initial oxidation state of the materials is conducted with cyclic voltammetry displayed in Figure 7b. The first cycle of the voltammograms for the non-fluorinated and fluorinated samples shows a similar behavior, whereas, in the case of a higher oxidation state following the fluorination, electrochemical activity at a higher potential is expected. The voltammetric profiles of the following cycles for the non-fluorinated and fluorinated materials (Figure 7c–e) display a single reduction peak, ramping up from 0.05 to 0.3 V vs. Li^+/Li during the first three cycles and maintained at 0.3 V for subsequent cycles. The voltammograms exhibit a single oxidation peak at 1.26 V vs. Li^+/Li for the first cycle, rising to 1.3 V vs. Li^+/Li for the following cycles. Finally, the electrochemical mechanism of the samples was confirmed to be identical using the galvanostatic intermittent titration pulsed technique (GITT in Figure S4). Figure S4a displays the potential profiles for the first discharge and charge of the three samples. The determination of the Li^+ diffusion (D_{Li^+}) within the active material is an important factor for the monitoring of the electrochemical reactions and their kinetics. Figure S4b shows a single step with the single step titration parameters τ , ΔE_t and ΔE_s illustrated. Assuming that the cell reaches stable potential at the end of each titration, the D_{Li^+} can be calculated using the simplified Fick's second law [58] (Equation (1)):

$$D_{\text{Li}^+} = \frac{4}{\tau \pi} \left(\frac{m_B V_M}{M_B A} \right)^2 \left(\frac{\Delta E_s}{\Delta E_t} \right)^2 \quad (1)$$

where M_B , V_M , m_B and A are the molecular weight, molar volume, mass of the material and its specific area, the latter being determined by BET measurements as mentioned above. Based on Equation (1), the D_{Li^+} can be calculated for each titration step and be expressed as a function of the potential. Figure S4c displays the evolution of the calculated D_{Li^+} for the non-fluorinated and fluorinated samples of Mn_3O_4 . During the discharge, the $\log_{10}(D_{Li^+})$ coefficient values range from -10 to -13.5 for all samples. The order of magnitude of the samples is overall similar; however, the precise D_{Li^+} values cannot be directly compared for the samples, as Equation (1) requires the experimentally determined $(mB/A)^2$, which can affect the comparison of calculated values for two different samples. The evolution of D_{Li^+} compared to the potential is more reliable information to be extracted from GITT measurements performed on different samples. This evolution was shown to be similar for all the samples; the first broad electrochemical mechanism can be identified for potentials ranging from 0.8 to 0.3 V vs. Li^+/Li , which has been attributed to the first discharge formation of the SEI and to a possible conversion of Mn_3O_4 to form MnO and Li_2O [59].

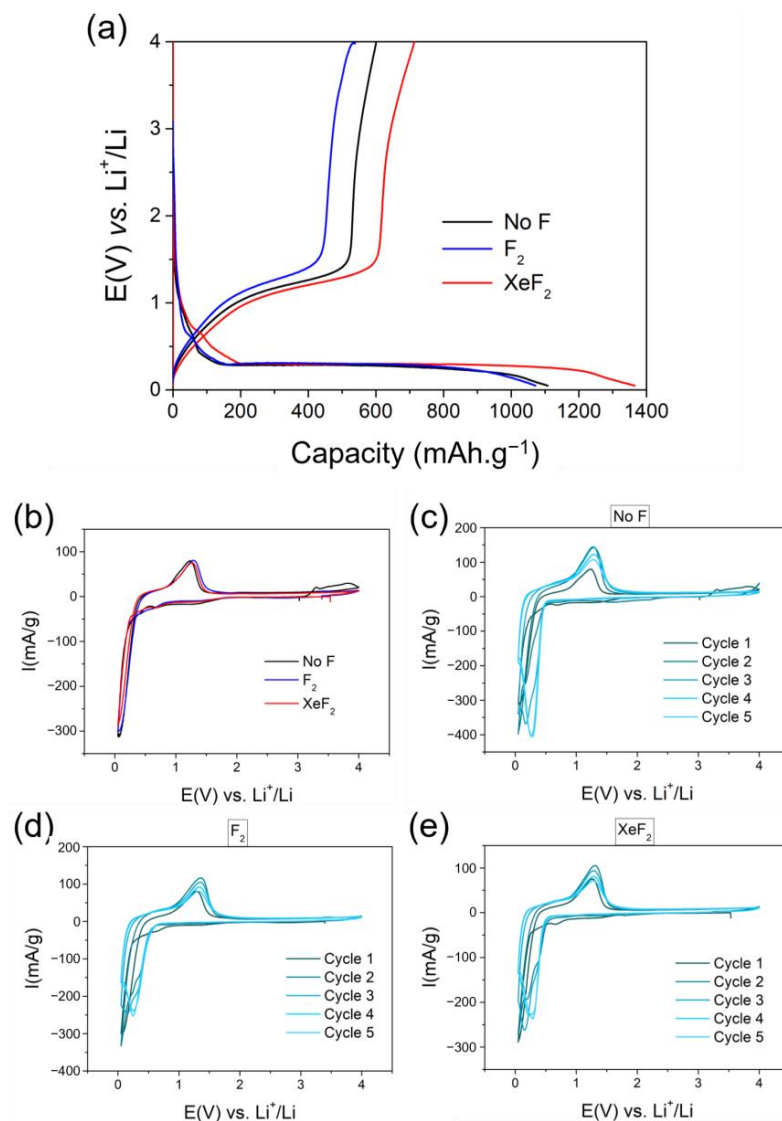


Figure 7. (a) First galvanostatic discharge and charge of the non-fluorinated and fluorinated samples at $D/20$ (46.85 mA g^{-1}) current density. (b) First voltammograms of the samples at 0.05 mV s^{-1} scan rate. (c–e) First five voltammograms for the respective samples: Mn_3O_4 , Mn_3O_4 fluorinated by F_2 and Mn_3O_4 fluorinated by XeF_2 at room temperature and between 0.05 and 4 V vs. Li^+/Li .

This first mechanism originates and terminates at the same potentials for all the samples. A second mechanism located at the same potential and centered at 0.23 V vs. Li⁺/Li, attributed to the conversion of Mn₃O₄ or previously formed MnO to Mn(0) and Li₂O, is also identical to all the samples, indicating a similar mechanism, as modified ligand chemistry is expected to affect the evolution of the D_{Li+} [60]. These results indicate that the fluorination by F₂ or XeF₂ of the samples does not affect the electrochemical mechanism of Mn₃O₄, the fluorination, therefore, affects the interface of the active material rather than its structure or metal-ligand bonding, as evidenced previously by physicochemical characterizations.

As discussed above with XPS measurements, the surface fluorination is particularly pronounced after F₂ fluorination. However, its electrochemical behavior does not seem to be affected (Figure 7a,b,d), indicating that the surface modification does not induce an improper interphase with the electrolyte, which would lead to a voltage polarization of the galvanostatic profile and a shift of the reduction peak to lower potentials in CV. The conservation of the electrochemical interphase with the electrolyte is further investigated by EIS, displayed in Figure 8a, with Nyquist plots of the non-fluorinated and fluorinated samples. All the materials showed a similar behavior consisting of a semicircle in the high-frequency region followed by a slope in the low-frequency region. The Nyquist plots were fitted using the equivalent circuit model displayed in Figure 8a. The very high-frequency region is composed of a resistance (Rs) attributed to the resistance of the electrolyte followed by the semicircle in the high-frequency region attributed to the charge transfer resistance (Rct1) at the interphase between the electrolyte and the active material. Finally, the slope in the low-frequency region represents the constant phase element CPE2 accounting for the Li⁺ diffusion within the electrode. All fitting parameters and relative errors for each fit are provided in Table S1. As the electrolyte (LP40) and separators were the same for these measurements, the Rs values fitted are on the same order of magnitude (21.74; 25.87 and 20.36 Ω for the non-fluorinated, fluorinated with F₂ and fluorinated with XeF₂ samples, respectively). The Rct1 values of the non-fluorinated and fluorinated with F₂ samples were very close (289.76 and 253.53 Ω, respectively), further confirming that the surface modification of the Mn₃O₄ particles observed by XPS does not affect the electrochemical interphase with the electrolyte. However, the sample fluorinated with XeF₂ experienced a severe increase in Rct resistance (360.24 Ω) compared to the non-fluorinated sample. This increase in charge transfer resistance could originate from the removal of the poorly ordered carbon in the bulk of the material, as evidenced by Raman spectroscopy in Figure 5, increasing the initial charge transfer resistance. Indeed, carbon coating of active materials particles is known to lower the charge transfer resistance [61,62], but in some cases, it can also affect the reversibility of conversion-type materials, especially Mn-based conversion materials that can experience several conversion mechanisms due to the numerous stable oxidation states of Mn [63].

Figure 8b displays the Nyquist plots of the cells assembled with the three samples after a discharge to 0.05 V vs. Li⁺/Li. The shape of the plots is different before the discharge, as a second interface, modeled by a second semicircle, is required to correctly fit the plots. Additionally, the low-frequency Li⁺ diffusion region is now fitted by a Warburg element W0 due to the angle of the slope closer to 45° compared to the samples before discharge with a slope angle closer to 90°. The electrolyte resistances of the fitted samples (25.11, 29.12 and 24.75 for No F, F₂ and XeF₂ respectively) show little variation compared to the EIS data before cycling—a small increase of ca. 4 Ohm was noticed, which can be attributed to a partial degradation of the electrolyte during the reduction mechanism. The emergence of a second semicircle after a discharge is usually attributed to the SEI contribution in the high-frequency area; however, the first semicircle in Figure 8b is closely related in frequency to the semicircle in Figure 8a. Therefore, the first semicircle in Figure 8b is considered

to be the charge transfer mechanism of the active material and the second semicircle at lower frequencies to an additional resistive interface for the active material. The Nyquist plots thus best fit using the equivalent circuit presented in the inset of Figure 8b. This modified Randle circuit with two components has been proposed by Hosseini and Zardari for the electrocatalysis of ORR (oxygen reduction reaction), displaying a two-step reduction process [64]. In our case, the two-step reduction processes can be attributed to two different Mn-based populations at low potential due to heterogeneous reduction reactions, possibly involving the non-ordered carbon from the synthesis. All fitting values for the discharged samples are provided in Table S2.

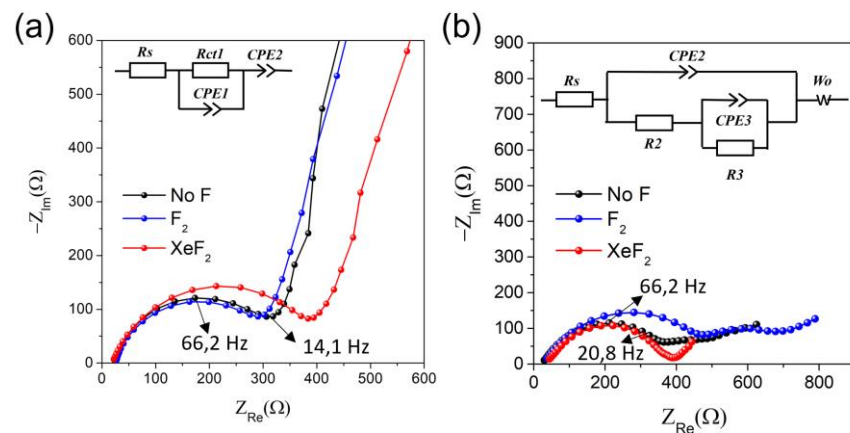


Figure 8. Nyquist plot of the different electrode materials (a) before and (b) after discharge with the equivalent circuits used for fitting parameters in the inset. Frequency data are provided for the No F sample for comparison purposes.

Assuming the above, the charge transfer resistance of the non-fluorinated and fluorinated with F_2 samples substantially increased by ca. 14.5 and 75%, respectively, while the sample fluorinated with XeF_2 decreased its charge transfer resistance by ca. 22%. Moreover, the second interface resistance is significantly lower for the XeF_2 sample (136.6, 160.4 and 43.08 for No F, F_2 and XeF_2 , respectively). This suggests that the fluorination process and the electrochemical aftermath strongly affect the interfacial properties of Mn_3O_4 active material and its reversibility. The additional conversion material originating from the reduction of Mn_3O_4 in its environment (i.e., the presence of poorly ordered carbon) can thus lead to a lowered reversibility of the active material.

Figure 9a displays the performance of the materials in prolonged galvanostatic cycling at a current density of D/20 (46.85 mA g^{-1}). The evolution of capacities upon cycling shows no improvement for the Mn_3O_4 sample after fluorination with F_2 , consistently with the similar XRD, Raman, FTIR and EIS profiles. However, the Mn_3O_4 fluorinated by XeF_2 shows increased performance as early as the first cycles, retaining a reversible capacity of 270 mAh g^{-1} at 66 cycles. For the Mn_3O_4 fluorinated with XeF_2 , the reversible capacity rapidly increases after 66 cycles, arriving at the theoretical capacity of graphite (i.e., 372 mAh g^{-1}) at 96 cycles. The improvement of the capacity for the sample fluorinated by XeF_2 could be related to the beneficial removal of the poorly organized carbon within the sample, which can interact with the reduction products (i.e., Li_2O and $Mn(0)$) at low potential, as evidenced by EIS measurements above, affecting the reversibility of the Mn_3O_4 electrochemical mechanism. The gradual loss in reversibility of Mn_3O_4 is evidenced by the decay in coulombic efficiency for the non-fluorinated and fluorinated with F_2 samples, dropping below 90% at the 50th cycle, while the sample fluorinated with XeF_2 retains a coulombic efficiency close to 100%.

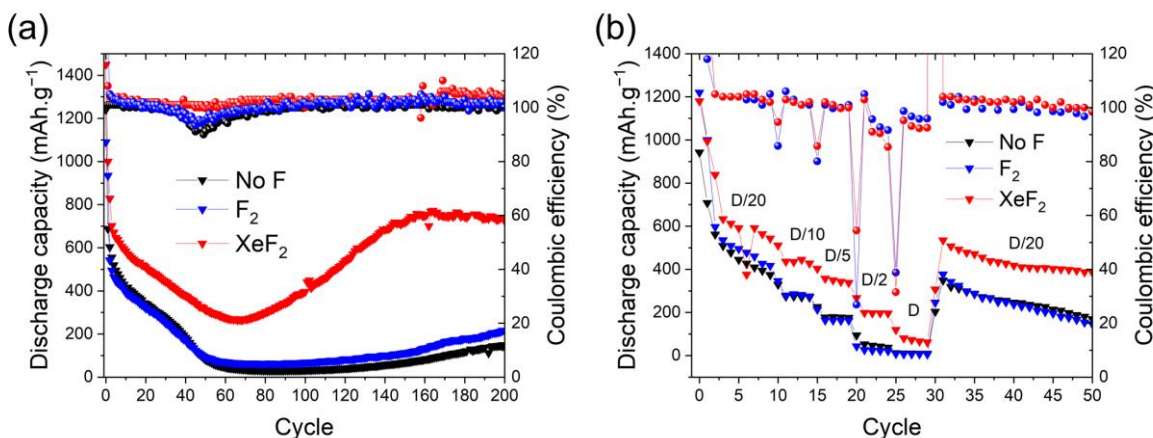


Figure 9. Evolution of the discharge capacity (left-hand side) and coulombic efficiency (right-hand side) of the non-fluorinated (No F, black curve), fluorinated with F₂ (F₂, blue curve) and fluorinated with XeF₂ (XeF₂, red curve) samples. (a) At D/20 current density (46.85 mA g⁻¹), prolonged galvanostatic cycling. (b) Rate performance with ten initial cycles at D/20 following five cycles at D/10 and D/5; D/2, D/1 and 20 cycles at D/20; and between 0.05 and 4.3 V vs. Li⁺/Li at room temperature.

The discharge capacity of the sample fluorinated with F₂ then further increases up to 750 mAh g⁻¹ at 160 cycles and remains stable for the subsequent cycles. An increase in capacity upon cycling is also observed for the samples without fluorination or after fluorination with F₂ gas but at a lower extent and after prolonged cycling (ca. 200 mAh g⁻¹ after 200 cycles) when compared to the samples fluorinated by XeF₂. This increase in capacity upon prolonged cycling for Mn₃O₄ has been reported by other authors [65,66] and studied in detail by Ma et al. [59]. They explain that an initial capacity fading is observed as the cycle number increases due to a lowered reduction potential. We also experienced this drop in reduction potential up to 40 cycles, as pictured in Figure S3. The origin of the voltage drop, according to Ma et al., is an ongoing reduction of the electrolyte, catalyzed by the Mn metal formed during the conversion process, increasing the charge transfer resistance of the electrode. Based on our study, and particularly on the EIS measurements, the presence of undesired and poorly organized carbon near the metallic Mn at the end of the reduction would also lead to a pronounced interface formation, thus lowering the accessible manganese species for the subsequent cycles. This degradation process will ultimately stop once the interface is finally formed, leading to a stabilization of the capacity. However, a poorly formed interface will negatively affect the performance of the electrode and will hinder its ability to increase its capacity upon cycling, as described below.

The origin of the gain in performance has been attributed by Ma et al. [59] to a higher oxidation state attained for manganese upon cycling due to a favorable electrode configuration. They stated that an adequate nano structuration of Mn₃O₄ particles or a favored electrical contact between Mn₃O₄ particles and a conductive network (e.g., nano-structured conductive carbon) is required for observing a gain in capacity upon cycling. In 2017, Cao et al. [67] showed that a proper mixing of Mn₃O₄ with Super-P carbon additive can effectively form MnO–C bonds with improved reversibility of the Mn₃O₄ redox mechanisms. The authors stressed the importance of proper mixing to obtain the MnO–C bonds, while improper MnO–C mixing resulted in lowered reversibility of the Mn₃O₄ particles. This increase in capacity is not only a phenomenon related to Mn₃O₄, as it has been observed in other oxides with a spinel structure, such as ZnMn₂O₄ [68], MnFe₂O₄ [69] and Fe₃O₄ [70]. For these materials, the nano structuration of the active materials or favored contact with conductive carbon is also highlighted.

According to our results, the presence of poorly organized carbon resulting from the synthesis of Mn_3O_4 negatively affects its electrochemical reversibility. Removing this carbon, thanks to the fluorination with XeF_2 , could lead to favored reversibility at higher oxidation states of the manganese oxide by lowering the undesirable reactions at low potential with the conversion products and residual carbon. This is supported by the galvanostatic profiles in Figure S3, showing that the excess capacity between cycle 40 and cycle 160 for the Mn_3O_4 (XeF_2) sample mainly originates from the capacity obtained above: 0.4 V vs. Li^+/Li .

Figure 9b shows the performance rate of the materials for different current densities. As a conversion material, Mn_3O_4 suffers from large irreversibility during the first cycles due to important volume expansion, reactivity or solubility of the conversion products with the electrolyte and particle loss of contact with the electrode's current collector. Five first cycles are thus necessary in order to attain decent reversibility for the cells prior to performing C-rate measurements [12,34]. The choice of five stabilizing cycles is adequate with the previously observed evolution by cyclic voltammetry in Figure 7, or by galvanostatic cycling in Figure 9a, where a capacity fading slope reaches linearity after five cycles. The obtained discharge capacities considered for the corresponding current densities are thus monitored after the fifth cycle. The current density was gradually increased after steps of five cycles, ranging from D/20, D/10, D/5, D/2 to D (46.85, 93.7, 187.4, 468.5 and 937 mA g^{-1} respectively), with the evolution of the capacity as a percentage of the initial capacity (i.e., after the five stabilizing cycles, provided in Figure S5). As previously observed by prolonged galvanostatic cycling, the Mn_3O_4 and Mn_3O_4 fluorinated by F_2 samples show similar behavior in performances, indicating that the F_2 surface fluorination did not help improve the power performance of Mn_3O_4 . The Mn_3O_4 fluorinated with XeF_2 displays again improved performances for increased current densities, with capacities of 443, 358, 211 and 80 mA g^{-1} for the D/10, D/5, D/2 and D current density steps, while the Mn_3O_4 or Mn_3O_4 fluorinated with F_2 only achieved capacities of about 274, 187, 54.5 and 10.3 mA g^{-1} . Interestingly, none of the Mn_3O_4 samples exhibited capacity loss after the C-rate measurements, as the capacity of the 31st cycle (i.e., when lowering back the current density to the initial D/20 step) was almost similar to the capacity prior to the current density increase.

4. Conclusions

In this study, Mn_3O_4 nanoparticles were successfully synthesized by solid combustion synthesis (SCS). The obtained powder underwent two different fluorination mechanisms, molecular fluorination by F_2 gas on one side and a radical fluorination by XeF_2 on the other side, both aiming at a 5% molar ratio of fluorination. The physicochemical characterizations of the samples showed limited differences, maintaining the structure of Mn_3O_4 active material. However, the XeF_2 fluorination removed the poorly ordered carbon originating from the SCS synthesis. This carbon removal significantly improved the electrochemical performances of the Mn_3O_4 active material, with 750 mA g^{-1} reversible capacity obtained after 200 cycles at 46.85 mA g^{-1} , while an absence of fluorination or fluorination with F_2 only provided capacities below 200 mAh g^{-1} after prolonged cycling. Additionally, the XeF_2 fluorination allowed for Mn_3O_4 to reach reversible capacities at or above graphite (372 mAh g^{-1}) at current densities as high as 187.4 mA g^{-1} . This study shows the potential applications of XeF_2 as a purifying agent for the post-synthesis treatment for lithium-ion battery active material.

Supplementary Materials: The following supporting information can be downloaded at: <https://www.mdpi.com/article/10.3390/batteries11020053/s1>; Figure S1: Adsorption isotherms of Mn_3O_4 oxide nanoparticles (non fluorinated, fluorinated with XeF_2 and fluorinated with F_2); Figure S2. Full-pattern matching of Mn_3O_4 X-ray diffractograms of (a) pristine Mn_3O_4 , (b) Mn_3O_4 fluorinated with XeF_2 and (c) Mn_3O_4 fluorinated with F_2 ; Figure S3. Galvanostatic profiles of Mn_3O_4 (XeF_2) sample at $D/20$ (46.85 mA g^{-1}) current density for cycles 1; 10; 20; 40 and 160 highlighted in dotted red line; Figure S4. (a) GITT curves for the discharge and charge of the three Mn_3O_4 samples, with or without fluorination (b) Voltage versus time curve of a single discharge/relaxation GITT step; (c) evolution of the Li^+ diffusion coefficient in potential vs. Li^+/Li calculated by Fick's second law with the discharge GITT results of the three samples; Figure S5. Relative evolution of the mean capacity at each current density step of the C-rate experiments for the non-fluorinated and fluorinated Mn_3O_4 materials. The reference initial capacity was obtained by averaging the stabilized cycles six to ten, without taking into account the initial one to five cycles where large irreversibility of the conversion material is observed. Table S1. Fitting parameters for the EIS equivalent circuit of No F, F2 and XeF_2 samples before discharge; Table S2. Fitting parameters for the EIS equivalent circuit of No F, F2 and XeF_2 samples after discharge.

Author Contributions: B.C. and R.P. contributed equally to this work. Writing—original draft B.C. and R.P.; Writing—review and editing B.C., R.P., K.G. and S.P.; Investigation, Visualization, Formal analysis, Data curation, Methodology, B.C., R.P., D.F. and E.P.; Synthesis, Investigation, Methodology T.K.; Conceptualization, Project supervision S.P., M.E.-G. and K.G.; Funding acquisition, S.P. All authors have read and agreed to the published version of the manuscript.

Funding: This research was funded by the French National Research Agency, ANR-21-CE08-0025-01, Project INFINE.

Data Availability Statement: The data presented in this study are included in the article and the Supporting Information.

Conflicts of Interest: The authors declare no conflicts of interest. The funders had no role in the design of this study; in the collection, analyses or interpretation of the data; in the writing of the manuscript; or in the decision to publish the results.

References

1. Larcher, D.; Tarascon, J.-M. Towards Greener and More Sustainable Batteries for Electrical Energy Storage. *Nat. Chem.* **2015**, *7*, 19–29. [[CrossRef](#)] [[PubMed](#)]
2. Zhu, Z.; Jiang, T.; Ali, M.; Meng, Y.; Jin, Y.; Cui, Y.; Chen, W. Rechargeable Batteries for Grid Scale Energy Storage. *Chem. Rev.* **2022**, *122*, 16610–16751. [[CrossRef](#)] [[PubMed](#)]
3. Zhao, W.; Zhao, C.; Wu, H.; Li, L.; Zhang, C. Progress, Challenge and Perspective of Graphite-Based Anode Materials for Lithium Batteries: A Review. *J. Energy Storage* **2024**, *81*, 110409. [[CrossRef](#)]
4. Nzereogu, P.U.; Omah, A.D.; Ezema, F.I.; Iwuoha, E.I.; Nwanya, A.C. Anode Materials for Lithium-Ion Batteries: A Review. *Appl. Surf. Sci. Adv.* **2022**, *9*, 100233. [[CrossRef](#)]
5. Ferg, E.; Gummow, R.D.; De Kock, A.; Thackeray, M.M. Spinel Anodes for Lithium-Ion Batteries. *J. Electrochem. Soc.* **1994**, *141*, L147–L150. [[CrossRef](#)]
6. Courtel, F.M.; Duncan, H.; Abu-Lebdeh, Y.; Davidson, I.J. High Capacity Anode Materials for Li-Ion Batteries Based on Spinel Metal Oxides AMn_2O_4 (A = Co, Ni, and Zn). *J. Mater. Chem.* **2011**, *21*, 10206. [[CrossRef](#)]
7. Han, X.; Gui, X.; Yi, T.-F.; Li, Y.; Yue, C. Recent Progress of $NiCo_2O_4$ -Based Anodes for High-Performance Lithium-Ion Batteries. *Curr. Opin. Solid State Mater. Sci.* **2018**, *22*, 109–126. [[CrossRef](#)]
8. Thackeray, M.M.; David, W.I.F.; Bruce, P.G.; Goodenough, J.B. Lithium Insertion into Manganese Spinels. *Mat. Res. Bull.* **1983**, *18*, 461–472. [[CrossRef](#)]
9. Gu, X.; Yue, J.; Li, L.; Xue, H.; Yang, J.; Zhao, X. General Synthesis of MnO_x (MnO_2 , Mn_2O_3 , Mn_3O_4 , MnO) Hierarchical Microspheres as Lithium-Ion Battery Anodes. *Electrochim. Acta* **2015**, *184*, 250–256. [[CrossRef](#)]
10. Gao, J.; Lowe, M.A.; Abruña, H.D. Spongelike Nanosized Mn_3O_4 as a High-Capacity Anode Material for Rechargeable Lithium Batteries. *Chem. Mater.* **2011**, *23*, 3223–3227. [[CrossRef](#)]
11. Ponrouch, A.; Taberna, P.-L.; Simon, P.; Palacín, M.R. On the Origin of the Extra Capacity at Low Potential in Materials for Li Batteries Reacting through Conversion Reaction. *Electrochim. Acta* **2012**, *61*, 13–18. [[CrossRef](#)]

12. Wu, F.; Yushin, G. Conversion Cathodes for Rechargeable Lithium and Lithium-Ion Batteries. *Energy Environ. Sci.* **2017**, *10*, 435–459. [[CrossRef](#)]
13. Varma, A.; Mukasyan, A.S.; Rogachev, A.S.; Manukyan, K.V. Solution Combustion Synthesis of Nanoscale Materials. *Chem. Rev.* **2016**, *116*, 14493–14586. [[CrossRef](#)]
14. Carlos, E.; Martins, R.; Fortunato, E.; Branquinho, R. Solution Combustion Synthesis: Towards a Sustainable Approach for Metal Oxides. *Chem. A Eur. J.* **2020**, *26*, 9099–9125. [[CrossRef](#)]
15. Novitskaya, E.; Kelly, J.P.; Bhaduri, S.; Graeve, O.A. A Review of Solution Combustion Synthesis: An Analysis of Parameters Controlling Powder Characteristics. *Int. Mater. Rev.* **2021**, *66*, 188–214. [[CrossRef](#)]
16. Deganello, F.; Tyagi, A.K. Solution Combustion Synthesis, Energy and Environment: Best Parameters for Better Materials. *Prog. Cryst. Growth Charact. Mater.* **2018**, *64*, 23–61. [[CrossRef](#)]
17. Li, F.; Ran, J.; Jaroniec, M.; Qiao, S.Z. Solution Combustion Synthesis of Metal Oxide Nanomaterials for Energy Storage and Conversion. *Nanoscale* **2015**, *7*, 17590–17610. [[CrossRef](#)]
18. Arnold, T.; Harth, C.M.; Mühlé, J.; Manning, A.J.; Salameh, P.K.; Kim, J.; Ivy, D.J.; Steele, L.P.; Petrenko, V.V.; Severinghaus, J.P.; et al. Nitrogen Trifluoride Global Emissions Estimated from Updated Atmospheric Measurements. *Proc. Natl. Acad. Sci. USA* **2013**, *110*, 2029–2034. [[CrossRef](#)]
19. Nojiri, K. *Dry Etching Technology for Semiconductors*; Springer International Publishing: Berlin/Heidelberg, Germany, 2015.
20. Wong, M.; Moslehi, M.M.; Reed, D.W. Characterization of Wafer Cleaning and Oxide Etching Using Vapor-Phase Hydrogen Fluoride. *J. Electrochem. Soc.* **1991**, *138*, 1799–1802. [[CrossRef](#)]
21. Nakajima, T.; Watanabe, N. *Graphite Fluorides & Carbon Fluoride Compounds*; Springer: Berlin/Heidelberg, Germany, 1991.
22. Sharma, N.; Dubois, M.; Guérin, K.; Pischedda, V.; Radescu, S. Fluorinated (Nano)Carbons: CF_x Electrodes and CF_x -Based Batteries. *Energy Tech.* **2021**, *9*, 2000605. [[CrossRef](#)]
23. Chatenet, M.; Berthon-Fabry, S.; Ahmad, Y.; Guérin, K.; Colin, M.; Farhat, H.; Frezet, L.; Zhang, G.; Dubois, M. Fluorination and Its Effects on Electrocatalysts for Low-Temperature Fuel Cells. *Adv. Energy Mater.* **2023**, *13*, 2204304. [[CrossRef](#)]
24. Ahmad, Y.; Batisse, N.; Chen, X.; Dubois, M. Preparation and Applications of Fluorinated Graphenes. *C* **2021**, *7*, 20. [[CrossRef](#)]
25. Li, T.; Zhang, X.-Q.; Shi, P.; Zhang, Q. Fluorinated Solid-Electrolyte Interphase in High-Voltage Lithium Metal Batteries. *Joule* **2019**, *3*, 2647–2661. [[CrossRef](#)]
26. Nakajima, T.; Groult, H. *Advanced Fluoride-Based Materials for Energy Conversion*; Elsevier: Amsterdam, The Netherlands, 2015.
27. Cui, D.; Zheng, Z.; Peng, X.; Li, T.; Sun, T.; Yuan, L. Fluorine-Doped SnO_2 Nanoparticles Anchored on Reduced Graphene Oxide as a High-Performance Lithium Ion Battery Anode. *J. Power Sources* **2017**, *362*, 20–26. [[CrossRef](#)]
28. Deng, Z.; He, M.; Feng, Y.; Xiong, D. A Fluorine-Doped MnFe_2O_4 Nanorod/Carbon Composite as an Anode Material for High-Performance Lithium-Ion Batteries. *Int. J. Electrochem. Sci.* **2020**, *15*, 4203–4217. [[CrossRef](#)]
29. Zhao, J.; Liao, L.; Shi, F.; Lei, T.; Chen, G.; Pei, A.; Sun, J.; Yan, K.; Zhou, G.; Xie, J.; et al. Surface Fluorination of Reactive Battery Anode Materials for Enhanced Stability. *J. Am. Chem. Soc.* **2017**, *139*, 11550–11558. [[CrossRef](#)]
30. Gervillié, C.; Dubois, M.; El-Ghazzi, M.; Berthon-Fabry, S.; Boisard, A.; Labbé, J.; Guérin, K. Optimized Electrode/Electrolyte Interface of MWCNT/ SnO_2 Composite through Gas–Solid Fluorination. *ACS Appl. Mater. Interfaces* **2021**, *13*, 28150–28163. [[CrossRef](#)]
31. Palaniyandy, N.; Nkosi, F.P.; Raju, K.; Ozoemena, K.I. Fluorinated Mn_3O_4 Nanospheres for Lithium-Ion Batteries: Low-Cost Synthesis with Enhanced Capacity, Cyclability and Charge-Transport. *Mater. Chem. Phys.* **2018**, *209*, 65–75. [[CrossRef](#)]
32. Le Bail, A.; Duroy, H.; Fourquet, J.L. Ab-Initio Structure Determination of LiSbWO_2 by X-Ray Powder Diffraction. *Mater. Res. Bull.* **1988**, *23*, 447–452. [[CrossRef](#)]
33. Rodríguez-Carvajal, J. Recent Advances in Magnetic Structure Determination by Neutron Powder Diffraction. *Phys. B Condens. Matter* **1993**, *192*, 55–69. [[CrossRef](#)]
34. Li, J.; Hwang, S.; Guo, F.; Li, S.; Chen, Z.; Kou, R.; Sun, K.; Sun, C.-J.; Gan, H.; Yu, A.; et al. Phase Evolution of Conversion-Type Electrode for Lithium Ion Batteries. *Nat. Commun.* **2019**, *10*, 2224. [[CrossRef](#)] [[PubMed](#)]
35. Thommes, M.; Kaneko, K.; Neimark, A.V.; Olivier, J.P.; Rodriguez-Reinoso, F.; Rouquerol, J.; Sing, K.S.W. Physisorption of Gases, with Special Reference to the Evaluation of Surface Area and Pore Size Distribution (IUPAC Technical Report). *Pure Appl. Chem.* **2015**, *87*, 1051–1069. [[CrossRef](#)]
36. Jarosch, D. Crystal Structure Refinement and Reflectance Measurements of Hausmannite, Mn_3O_4 . *Mineral. Petrol.* **1987**, *37*, 15–23. [[CrossRef](#)]
37. Sasaki, S.; Fujino, K.; Takéuchi, Y. X-Ray Determination of Electron-Density Distributions in Oxides, MgO , MnO , CoO , and NiO , and Atomic Scattering Factors of Their Constituent Atoms. *Proc. Jpn. Acad., Ser. B* **1979**, *55*, 43–48. [[CrossRef](#)]
38. Grzybowski, A.K.; Tate, S.S.; Datta, S.P. Magnesium and Manganese Complexes of Citric and Lsocitric Acids. *J. Chem. Soc. A* **1970**, 241–245. [[CrossRef](#)]
39. Baur, W.H.; Khan, A.A. Rutile-Type Compounds. IV. SiO_2 , GeO_2 and a Comparison with Other Rutile-Type Structures. *Acta Cryst. B* **1971**, *27*, 2133–2139. [[CrossRef](#)]

40. Bandemehr, J.; Stoll, C.; Heymann, G.; Ivlev, S.I.; Karttunen, A.J.; Conrad, M.; Huppertz, H.; Kraus, F. The Crystal Structure of MnF_3 Revisited. *Z. Anorg Allg Chem.* **2020**, *646*, 882–888. [[CrossRef](#)]
41. De Windt, S.; Auvergniot, J.; Cabelguen, P.-E.; Gschwind, F.; Dubois, M.; Guerin, K. Strategies to Achieve Stable Manganese Oxyfluorides by Tuning the Reactivity of Pure Molecular Fluorine. *Inorg. Chem.* **2023**, *62*, 19612–19621. [[CrossRef](#)]
42. Ardizzone, S.; Bianchi, C.L.; Tirelli, D. Mn_3O_4 and Gamma- $MnOOH$ Powders, Preparation, Phase Composition and XPS Characterisation. *Colloids Surf. A Physicochem. Eng. Asp.* **1998**, *134*, 305–312. [[CrossRef](#)]
43. Galakhov, V.R.; Demeter, M.; Bartkowski, S.; Neumann, M.; Ovechkina, N.A.; Kurmaev, E.Z.; Lobachevskaya, N.I.; Mukovskii, Y.M.; Mitchell, J.; Ederer, D.L. Mn 3s Exchange Splitting in Mixed-Valence Manganites. *Phys. Rev. B* **2002**, *65*, 113102. [[CrossRef](#)]
44. Ebner, J.R.; McFadden, D.L.; Walton, R.A. The X-Ray Photoelectron Spectra of Inorganic Molecules. XI. Fluorine 1s Binding Energies in Metal Fluorides. *J. Solid State Chem.* **1976**, *17*, 447–449. [[CrossRef](#)]
45. Lutz, H.D.; Mijller, B.; Steiner, H.J. Lattice Vibration Spectra. LIX. Single Crystal Infrared and Raman Studies of Spinel Type Oxides. *J. Solid State Chem.* **1991**, *90*, 54–60. [[CrossRef](#)]
46. Rani, B.J.; Ravina, M.; Ravi, G.; Ravichandran, S.; Ganesh, V.; Yuvakkumar, R. Synthesis and Characterization of Hausmannite (Mn_3O_4) Nanostructures. *Surf. Interfaces* **2018**, *11*, 28–36. [[CrossRef](#)]
47. Julien, C.M.; Massot, M.; Poinsignon, C. Lattice Vibrations of Manganese Oxides Part I. Periodic Structures. *Spectrochim. Acta Part A Mol. Biomol. Spectrosc.* **2004**, *60*, 689–700. [[CrossRef](#)]
48. Mironova-Ulmane, N.; Kuzmin, A.; Grube, M. Raman and Infrared Spectromicroscopy of Manganese Oxides. *J. Alloys Compd.* **2009**, *480*, 97–99. [[CrossRef](#)]
49. Porto, S.P.S.; Fleury, P.A.; Damen, T.C. Raman Spectra of TiO_2 , MgF_2 , ZnF_2 , FeF_2 , and MnF_2 . *Phys. Rev.* **1967**, *154*, 522–526. [[CrossRef](#)]
50. Tuinstra, F.; Koenig, J.L. Raman Spectrum of Graphite. *J. Chem. Phys.* **1970**, *53*, 1126–1130. [[CrossRef](#)]
51. Batisse, N.; Guérin, K.; Dubois, M.; Hamwi, A.; Spinelle, L.; Tomasella, E. Fluorination of Silicon Carbide Thin Films Using Pure F_2 Gas or XeF_2 . *Thin Solid Film.* **2010**, *518*, 6746–6751. [[CrossRef](#)]
52. Nansé, G.; Papirer, E.; Fioux, P.; Moguet, F.; Tressaud, A. Fluorination of Carbon Blacks: An X-Ray Photoelectron Spectroscopy Study: I. A Literature Review of XPS Studies of Fluorinated Carbons. XPS Investigation of Some Reference Compounds. *Carbon* **1997**, *35*, 175–194. [[CrossRef](#)]
53. Gupta, V.; Nakajima, T.; Ohzawa, Y.; Žemva, B. A Study on the Formation Mechanism of Graphite Fluorides by Raman Spectroscopy. *J. Fluor. Chem.* **2003**, *120*, 143–150. [[CrossRef](#)]
54. Hamwi, A.; Daoud, M.; Cousseins, J.C. Graphite Fluorides Prepared at Room Temperature 1. Synthesis and Characterization. *Synth. Met.* **1988**, *26*, 89–98. [[CrossRef](#)]
55. Malm, J.G.; Selig, H.; Jortner, J.; Rice, S.A. The Chemistry of Xenon. *Chem. Rev.* **1965**, *65*, 199–236. [[CrossRef](#)]
56. Tramsek, M.; Zemva, B. Synthesis, Properties and Chemistry of Xenon(II) Fluoride. *Acta Chim. Slov.* **2007**, *38*, 105–116. [[CrossRef](#)]
57. Wang, A.; Kadam, S.; Li, H.; Shi, S.; Qi, Y. Review on Modeling of the Anode Solid Electrolyte Interphase (SEI) for Lithium-Ion Batteries. *NPJ Comput. Mater.* **2018**, *4*, 15. [[CrossRef](#)]
58. Takahashi, T.; Esaka, T. Determination of the Kinetic Parameters of Mixed-Conducting Electrodes and Application to the System Li_3Sb . *J. Electrochem. Soc.* **1977**, *124*, 1569–1578. [[CrossRef](#)]
59. Ma, F.; Yuan, A.; Xu, J. Nanoparticulate Mn_3O_4 /VGCF Composite Conversion-Anode Material with Extraordinarily High Capacity and Excellent Rate Capability for Lithium Ion Batteries. *Appl. Mater. Interfaces* **2014**, *6*, 18129–18138. [[CrossRef](#)]
60. Jiang, J.; Zhang, R.; Sun, T.; Guo, J.; Liu, J.; Cheng, P.; Shi, W. Boosting the Lithium-Ion Transport Kinetics of Sn-Based Coordination Polymers through Ligand Aromaticity Manipulation. *Inorg. Chem.* **2023**, *62*, 16609–16616. [[CrossRef](#)]
61. Xu, S.; Hou, X.; Wang, D.; Ztin, L.; Zhou, J.; Hou, Y.; Mann, M. Insights into the Effect of Heat Treatment and Carbon Coating on the Electrochemical Behaviors of SiO Anodes for Li-Ion Batteries. *Adv. Energy Mater.* **2022**, *12*, 2200127. [[CrossRef](#)]
62. Iarchuk, A.R.; Nikitina, V.A.; Karpushkin, E.A.; Sergeyev, V.G.; Antipov, E.V.; Stevenson, K.J.; Abakumov, A.M. Influence of Carbon Coating on Intercalation Kinetics and Transport Properties of $LiFePO_4$. *ChemElectroChem* **2019**, *6*, 5090–5100. [[CrossRef](#)]
63. Zhao, Z.; Tian, G.; Sarapulova, A.; Melinte, G.; Gómez-Urbano, J.L.; Li, C.; Liu, S.; Welter, E.; Etter, M.; Dsoke, S. Mechanism Study of Carbon Coating Effects on Conversion-Type Anode Materials in Lithium-Ion Batteries: Case Study of $ZnMn_2O_4$ and ZnO - MnO Composites. *ACS Appl. Mater. Interfaces* **2019**, *11*, 29888–29900. [[CrossRef](#)]
64. Hosseini, M.G.; Zardari, P. Electrocatalytical Study of Carbon Supported Pt, Ru and Bimetallic Pt–Ru Nanoparticles for Oxygen Reduction Reaction in Alkaline Media. *Appl. Surf. Sci.* **2015**, *345*, 223–231. [[CrossRef](#)]
65. Akhtar, M.S.; Bui, P.T.M.; Li, Z.-Y.; Yang, O.-B.; Paul, B.J.; Kim, S.; Kim, J.; Rai, A.K. Impact of Porous Mn_3O_4 Nanostructures on the Performance of Rechargeable Lithium Ion Battery: Excellent Capacity and Cyclability. *Solid State Ion.* **2019**, *336*, 31–38. [[CrossRef](#)]
66. Huang, S.-Z.; Cai, Y.; Jin, J.; Liu, J.; Li, Y.; Yu, Y.; Wang, H.-E.; Chen, L.-H.; Su, B.-L. Hierarchical Mesoporous Urchin-like Mn_3O_4 /Carbon Microspheres with Highly Enhanced Lithium Battery Performance by in-Situ Carbonization of New Lamellar Manganese Alkoxide (Mn-DEG). *Nano Energy* **2015**, *12*, 833–844. [[CrossRef](#)]

67. Cao, L.; Wang, R.; Xu, Z.; Li, J.; Huang, J.; Li, R.; Li, K. Constructing Mn-O-C Bonds in Mn_3O_4 /Super P Composite for Superior Performance in Li-Ion Battery. *J. Electroanal. Chem.* **2017**, *798*, 1–8. [[CrossRef](#)]
68. Min, X.; Zhang, Y.; Yu, M.; Wang, Y.; Yuan, A.; Xu, J. A Hierarchical Dual-Carbon Supported $ZnMn_2O_4/C$ Composite as an Anode Material for Li-Ion Batteries. *J. Alloys Compd.* **2021**, *877*, 160242. [[CrossRef](#)]
69. Ghosh, S.; de Donder, T.; Gunnarsson, K.; Kumar, V.K.; Martha, S.K.; Svedlindh, P.; Kessler, V.G.; Seisenbaeva, G.A.; Pol, V.G. Investigating the Stable Operating Voltage for the $MnFe_2O_4$ Li-Ion Battery Anode. *Sus. Ener. Fuels* **2021**, *5*, 1904–1913. [[CrossRef](#)]
70. Yang, Y.; Li, J.; Chen, D.; Zhao, J. A Facile Electrophoretic Deposition Route to the $Fe_3O_4/CNTs/RGO$ Composite Electrode as a Binder-Free Anode for Lithium Ion Battery. *ACS Appl. Mater. Interfaces* **2016**, *8*, 26730–26739. [[CrossRef](#)]

Disclaimer/Publisher’s Note: The statements, opinions and data contained in all publications are solely those of the individual author(s) and contributor(s) and not of MDPI and/or the editor(s). MDPI and/or the editor(s) disclaim responsibility for any injury to people or property resulting from any ideas, methods, instructions or products referred to in the content.